Progress In Electromagnetics Research C, Vol. 88, 117–131, 2018

A Design of Broadband and Low-Loss Multilayer Antireflection Coating in THz Region

Hsin-Yu Yao, Zih-Yu Chen, and Tsun-Hsu Chang*

Abstract—An approach to the design and the realization of a broadband multilayer anti-reflection (AR) coating with high transmission is proposed in this study. A binominal multi-section transformer is employed to efficiently determine the thickness and the refractive index of each matching layer, while those layers can be further realized by doping different fractions of subwavelength-size silicon powders (for relatively-high-index layers) or air pores (for relatively-low-index layers) into the low-loss HDPE polymer host. Based on this scheme, we design a ten-layer AR coating for widely used silicon wafer. The designed AR coatings are double-sided integrated with a 375-μm-thick silicon wafer, which can enhance the overall THz transmission to higher than 95.00% from 0.250 THz to 0.919 THz (114.46% fractional bandwidth) for either TE-polarized or TM-polarized THz beam incident from an arbitrary angle below 50°.

1. INTRODUCTION

A low-loss antireflection (AR) coating is able to reduce light reflection at an interface between two different materials or devices, and thus it is capable of maximizing total transmission [1]. Various practical designs have been developed for visible and infrared regions [1–4]. Recently, this technique is widely used in terahertz (THz) region to enhance the transmission efficiency of devices, such as windows [5], filters [6, 7], photoconductive switching antennae that use semiconductor substrates [8] and lenses [9]. Among these devices, silicon has been widely used due to its exceptional electrical and optical properties [10]. Since the refractive index of silicon (around 3.4) is much higher than that of air in THz region, the Fresnel reflection at air-silicon interface reaches 30% [11], which significantly lowers the transmission efficiency of these silicon-based devices and might complicate the optical path in experiment due to strong multiple reflections. Thus, there is an urgent need for developing a high-efficiency AR coating in the THz region.

Single-layer AR coating that utilizes destructive interference to eliminate overall reflection is the most common and easy way [11, 12]. The thickness of single AR layer is selected as a quarter wavelength, while its refractive index should be chosen at $\sqrt{n_L}$, intermediate between one (the index of air) and n_L (the index of the material under match). As demonstrated in [11], the THz transmission from silicon was enhanced to 80% ranging from 1.658 THz to 2.199 THz (28.05% fractional bandwidth, which is defined by the ratio of the available spectral bandwidth to its center frequency). However, since only a single wavelength was matched, the valid bandwidth was quite limited, making this kind of design inadequate for broadband THz experiment [13].

In order to further broaden the bandwidth, multilayer AR coating has been developed [14–16], in which the refractive indices of matching layers gradually vary from the index of air to that of the material under match, facilitating the reduction of Fresnel reflection at each interface. In Ref. [14], the multilayer AR coating was demonstrated to significantly reduce the reflection loss of silicon to below 20% from

Received 26 July 2018, Accepted 5 November 2018, Scheduled 15 November 2018
* Corresponding author: Tsun-Hun Chang (thschang@phys.nthu.edu.tw).
The authors are with the Department of Physics, National Tsing Hua University, Hsinchu 300, Taiwan, R.O.C.

1.199 THz to 2.518 THz (70.97% fractional bandwidth), showing nearly triple bandwidth compared to the case employed single-layer AR coating [11]. On the parallel front, sub-wavelength relief structures implemented by either micro-pyramid [17–20] or biomimetic nano-tip [21] were developed. These coatings replace the conventional planar-type matching layer by sub-wavelength tapered microstructure made by the same material of the target under match. Analogous to the concept of multilayer AR coating [14–16], this method effectively forms a gradient index profile for reducing impedance mismatching and minimizing overall reflection. By coating the micro-pyramid structures with a period of 30 μm on the front surface of a silicon wafer [17], the reflectivity was restrained to below 20% with a broad band ranging from 1.670 THz to 3.076 THz (59.25% fractional bandwidth). Even though both the multilayer AR coating and the subwavelength relief structure show promising performance in the reduction of THz reflection with broad bandwidth, these two mechanisms still suffer from serious difficulties in fabrication. For the multilayer structure, it is difficult to find various low-loss dielectrics in nature that exactly possess the required refractive indices, while the relief-structure AR coating is only feasible for limited materials, which exhibit a low loss in the THz regime and the capability of being grown/etched into tapered structure in sub-wavelength dimension. In addition, both of these AR methods lack powerful design guidelines.

Recently, ultra-thin metasurfaces are of widespread interests due to their potential ability to significantly improve AR performance. Various metasurfaces were developed, such as highly roughened surfaces [22] and patterned metallic [23, 24] and dielectric [25, 26] metasurfaces. The surface roughness of a highly roughened system is usually much larger than the operating wavelength [22], resulting in severe internal scattering and strong light trapping effect. Absorption (reflection) is therefore strongly enhanced (suppressed). This feature should benefit the design of perfect absorber but go against "low-loss" AR coating, i.e., the main aim of this work. On the other hand, metasurfaces with subwavelength structures [23, 25, 26] can induce localized electric and magnetic resonances of the surface plasmon, which can control effective permittivity and permeability, respectively. Tailored permittivity and permeability facilitate impedance matching with free space, leading to low reflection. This concept seems like a novel idea to realize ultra-thin AR coatings in the THz band. However, the available bandwidth of such a device is relatively limited, and the absorption would be enhanced due to the nature of resonance.

In this study, we propose an alternative approach to the design and realization of a broadband multilayer AR coating with high transmission. To efficiently determine the thickness and the refractive index of each matching layer, a binominal multi-section transformer for impedance matching is employed. A design guideline is clearly described, the simplicity of which should spare the user from heavy numerical optimization for design [15]. To overcome the limitation in nature materials for realization, we suggest that the relatively high-index layers (refractive index $n > 1.530$) can be fabricated by doping subwavelength-size silicon powders ($n \cong 3.418$) into low-loss HDPE layer ($n \cong 1.530$), while the relatively low-index layers ($n < 1.530$) can be fabricated by doping subwavelength-size air pores ($n = 1.000$) into HDPE layer. Through tuning the doping ratios, a series of low-loss composites with various indices ranging from 1.000 to 3.418 can be fabricated, facilitating the realizations of some THz devices, such as multilayer AR coating and THz Bragg fiber [27, 28]. To the best of our knowledge, although the design concepts (impedance matching) and material concepts (polymer composites) have been widely used in many fields, the combination of them to efficiently design and realize a high-performance THz AR coating is proposed in this work for the first time. Based on this scheme, a design of broadband multilayer AR coating for silicon is proposed, which is able to significantly enhance the overall transmission power to more than 95.00% within 0.250 THz to 0.919 THz (114.46% fractional bandwidth) for either TE-polarized or TM-polarized THz waves incident at any angles below 50°. According to our sensitivity analysis, this design is not sensitive to the changes of the refractive index and thickness, indicating high stability and feasibility.

2. DESIGN GUIDELINE OF MULTILAYER ANTI-REFLECTION COATING

According to the Fresnel law of reflection, the larger the difference is between two refractive indices, the stronger the reflection is owing to severer impedance mismatching. There are two effective ways to suppress the Fresnel reflection: gradient index implemented on sufficient numbers of the discrete matching layer for lowering every interface reflection [14–16, 29, 30] and destructive interference [11, 12]

for eliminating the residual reflected waves. In the following, these two methods would be combined for design. As a THz wave transmits into a multilayer AR coating, it would bounce back and forth in every matching layer, forming sequences of consecutive reflection. In order to introduce destructive interference for canceling reflection, the thickness of each layer is selected as quarter wavelength for normal incidence [$d_j = \lambda_0/(4n_j)$, where λ_0 is the free-space wavelength chosen to match, and d_j is the thickness of j-th layer whose refractive index is n_j]. It suggests that at the design wavelength (λ_0) the first-order reflected echoes from any two adjacent interfaces must be out of phase [11, 12].

On the other hand, how the refractive index varies from layer to layer determines how broad the high-transmission band could be achieved. In the previous studies [15, 16, 29, 30], the index profiles were usually optimized by massive numerical simulations at the expense of long computation time and the lack of the understanding about underlying mechanism. To provide an efficient design guideline with the clear physical picture, we, therefore, adopt the binomial multi-section matching transformer [31] to determine the required refractive index of each matching layer, which ensures minimum reflection (high transmission) and maximally flat frequency response (low dispersion). Fig. 1 schematically illustrates the general configuration of N-layer AR coating integrated with a target substrate. The far-left region in Fig. 1 is air (incident region) with an index (n_0) of one, while the far-right region is the material under match with an index of n_L. The refractive index and the thickness of j-th matching layer are respectively denoted as n_j and d_j. It should be noted that these layers are assumed to be transversely semi-infinite so that the diffraction effect at their edges is neglected. This implies that propagating wave in every layer could be treated as TEM mode, exhibiting a propagation constant of $k_j = n_j\omega/c$, where ω is the carrier frequency of EM wave and c is the speed of light in vacuum. Besides, the dielectric losses of all matching layers are assumed to be negligible ($\mathrm{Im}[n_j] \ll \mathrm{Re}[n_j]$), and thus n_j is treated as a real number for simplicity. How dielectric loss affects the performance of the designed AR coating will be shown and discussed in Sections 5, 6 and 7. As explained above, the thickness of each layer is determined as quarter optical wavelength [$d_j = \lambda_0/(4n_j)$], leading to the same phase change [$\theta \equiv k_j d_j = \pi/2 \times (\omega/\omega_0)$, $\omega_0 = 2\pi c/\lambda_0$] for a plane wave having a single-pass trip between arbitrary two adjacent interfaces.

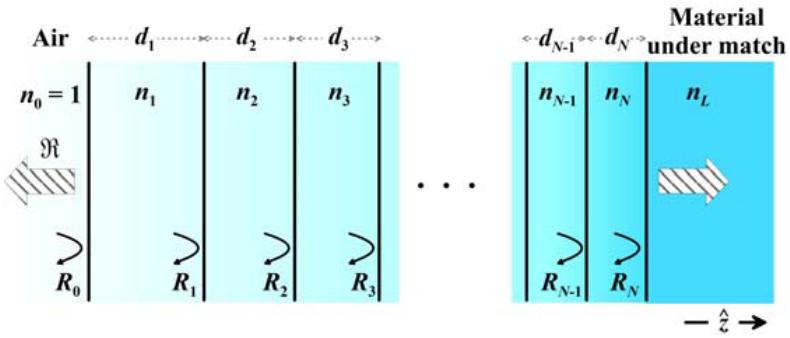

Figure 1. Schematic diagram of the substrate under match integrated with N-layer AR coating on a single side (air to target). Note the input region (air) and the target respectively lie on the far left and the far right, while the multilayer AR coating with a gradient index profile is embedded in between. The thickness and the refractive index of j-th layer are respectively denoted as d_j and n_j. The Fresnel reflection at the interface between j-th and $(j+1)$-th layers is denoted as R_j and the overall reflection is represented by $\Re$.

If the total number of matching layers is sufficient to form a slow-varying index profile ($n_L > n_N > n_{N-1} > \ldots > n_2 > n_1$), the Fresnel reflection at each interface (R_j) is supposed to be significantly suppressed, as may be seen from $R_j = (n_j - n_{j+1})/(n_j + n_{j+1})$ for $0 \le j \le N-1$ and $R_N = (n_N - n_L)/(n_N + n_L)$. The overall reflection ($\Re$), which essentially should be the superposition of all reflected echoes, now can be approximately expressed as

$$\Re(\theta) \approx \sum_{j=0}^{N} R_j e^{i\times(2j\theta)}. \tag{1}$$

In Eq. (1), we assume that only the first-order reflected waves have a contribution in $\Re$; in other words, all other higher-order multiple-reflection echoes that experience more than once interface reflection are neglected due to the small-reflection condition. The effect of these higher-order terms would be taken into account in actual performance analysis (Sections 5, 6 and 7). To ensure that the overall reflection is small, and its frequency response is as flat as possible, we let

$$\Re(\theta) = 2^{-N}\left(\frac{1-n_L}{1+n_L}\right)(1+e^{i\times 2\theta})^N, \tag{2}$$

which infers that the reflectivity ($|\Re(\theta)|^2$) and its first $N-1$ derivatives with respect to $\theta(\omega)$ would both drop to zero as operating at the design frequency ω_0 [$\theta(\omega_0) = \pi/2$]. Eq. (2) can be further expanded according to binominal expansion, yielding

$$\Re(\theta) = 2^{-N}\left(\frac{1-n_L}{1+n_L}\right)\sum_{j=0}^{N}\frac{N!}{(N-j)!j!}e^{i\times(2j\theta)}. \tag{3}$$

Substituting $R_j = (n_j - n_{j+1})/(n_j + n_{j+1})$ into Eq. (1) and comparing with Eq. (3) term-by-term, the following relation is obtained,

$$\frac{n_j - n_{j+1}}{n_j + n_{j+1}} = 2^{-N}\left(\frac{1-n_L}{1+n_L}\right)\frac{N!}{(N-j)!j!}. \tag{4}$$

Note that there are $N+1$ reflection coefficients [R_j with $j = 0, 1, \ldots, N$] in Eq. (1), while there are only N matching layers exhibiting degrees of freedom for design. Thus, the design rule described in Eq. (4) is certainly over constrained, which might result in serious errors. Such a dilemma could be fixed by using the approximation: $(n_j - n_{j+1})/(n_j + n_{j+1}) \simeq \ln(n_j/n_{j+1})/2$, as long as the index mismatching between any two adjacent layers is small enough. This implies

$$\ln(n_{j+1}) = \ln(n_j) + 2^{-N}\left[\frac{N!}{(N-j)!j!}\right]\ln(n_L). \tag{5}$$

The self-consistent recurrence relation shown in Eq. (5) finally enables us to determine the refractive index of $(j+1)$-th layer (n_{j+1}) based on the known index of j-th layer (n_j), starting with $j = 0$.

The fractional bandwidth ($\Delta f/f_0$) of the system with single-sided AR coating can be evaluated as follows. Assuming $|\Re_{\max}|$ is the maximum reflection that can be tolerated over the passband and ω_{low} corresponds to the lower edge of the passband (hence $\Delta f/f_0 \equiv 2(\omega_0 - \omega_{\text{low}})/\omega_0 = 2 - 4\theta_{\text{low}}/\pi$), Eq. (2) further implies

$$\frac{\Delta f}{f_0} = 2 - \frac{4}{\pi}\cos^{-1}\left\{\left[|\Re_{\max}|\left(\frac{n_L+1}{n_L-1}\right)\right]^{1/N}\right\}. \tag{6}$$

It should be noted that Eq. (6) is estimated under the assumptions of zero higher-order reflected waves and negligible losses of all dielectric layers. Therefore, the actual bandwidth in realistic case might be slightly different, which will be discussed in Section 5. According to Eq. (6), the required total numbers of layer (N_{req}) for achieving targeted fractional bandwidth ($\Delta f/f_0$) can be expressed as

$$N_{\text{req}} > \ln\left\{|\Re_{\max}|\left(\frac{n_L+1}{n_L-1}\right)\right\}\Big/\ln\left\{\cos\left[\frac{\pi}{4}\left(2-\frac{\Delta f}{f_0}\right)\right]\right\}. \tag{7}$$

3. DESIGN OF MULTILAYER ANTI-REFLECTION COATING

In this section, a multilayer AR coating for matching air ($n_0 = 1.000$) and silicon ($n_s = 3.418 + 3.817\times10^{-5}i$) at 0.550 THz (the central frequency, $\omega_0/2\pi$) is designed based on the proposed guideline. The index of silicon can be treated as a constant for the current operating band [32]. By setting the maximum reflection of single-side matched silicon ($|\Re_{\max}|$) below 5% with a fractional bandwidth ($\Delta f/f_0$) greater than 120%, Eq. (7) can be leveraged to determine the required total numbers of matching layer, which suggests $N_{\text{req}} \geq 10$. Therefore, N is chosen as 10 in the present design. The required index ($\text{Re}[n_j]$) and the thickness (d_j) of each matching layer are shown in Table 1. The

Table 1. Parameters of ten-layer AR coating. First, second and third rows: the thickness (d_j), the optimized refractive index (Re[n_j]), the corresponding extinction coefficient (Im[n_j]) of j-th matching layer, respectively. Fourth row: the suggested doping ratios of the subwavelength-size particles (air pores or silicon powders) in the HDPE layer for the realization of each matching layer. Note that the data shown in upper panel represent the volumetric doping ratios of air pores in HDPE (for the relatively-low-index layers #1 to #4), while those shown in the bottom panel are the volumetric doping ratios of silicon powders in HDPE (for the relatively-high-index layers #5 to #10).

jth-layer	1	2	3	4
d_j(μm)	136	135	127	110
Re[n_j]	1.001	1.013	1.069	1.235
Im[n_j] ($\times 10^{-4}$)	0.010	0.095	0.519	1.876
ζ_j (%)	99.7	97.2	85.4	53.0

jth-layer	5	6	7	8	9	10
d_j(μm)	86	63	49	43	40	39
Re[n_j]	1.589	2.150	2.766	3.194	3.371	3.412
Im[n_j] ($\times 10^{-4}$)	4.562	3.908	2.423	1.142	0.578	0.450
ζ_j (%)	4.2	39.4	70.4	89.7	97.4	99.1

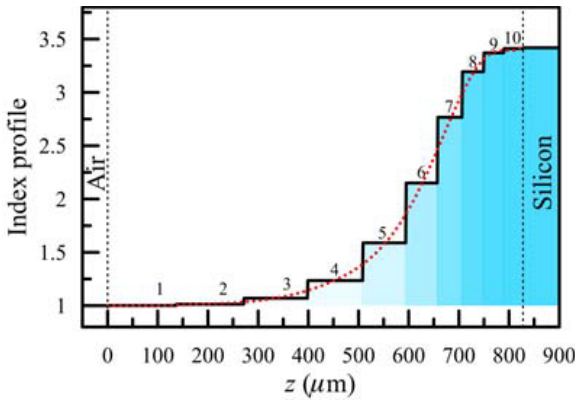

Figure 2. Discretized index profile of the ten-layer AR coating designed for matching air (at $z < 0\,\mu$m marked by left-hand-side vertical dashed line) and silicon (at $z > 828\,\mu$m marked by the right-hand-side vertical dashed line). The location of j-th matching layer is indicated by the number label j. Note that the lower the index of matching layer (closer to air), the thicker the thickness owing to the quarter-wavelength condition. The continuous red dotted curve is the 10th-degree polynomial regression; the coefficient of each term is listed in the main text.

corresponding index profile concerning the propagation direction ($\hat{z}$) is illustrated in Fig. 2, in which the location of each matching layer is individually specified. The continuous index profile (red dotted curve) is the 10th-degree polynomial regression fitted to the discretized index profile (black solid curve), described by

$$n(z) = \sum_{j=0}^{10} a_j z^j, \tag{8}$$

with $a_0 = 1.001$, $a_1 = -4.123 \times 10^{-5}\,\mu\text{m}^{-1}$, $a_2 = 4.350 \times 10^{-6}\,\mu\text{m}^{-2}$, $a_3 = -1.233 \times 10^{-7}\,\mu\text{m}^{-3}$, $a_4 = 1.561 \times 10^{-9}\,\mu\text{m}^{-4}$, $a_5 = -1.026 \times 10^{-11}\,\mu\text{m}^{-5}$, $a_6 = 3.872 \times 10^{-14}\,\mu\text{m}^{-6}$, $a_7 = -8.651 \times 10^{-17}\,\mu\text{m}^{-7}$,

$a_8 = 1.129\times10^{-19}\,\mu\text{m}^{-8}$, $a_9 = -7.912\times10^{-23}\,\mu\text{m}^{-9}$, and $a_{10} = 2.294\times10^{-26}\,\mu\text{m}^{-10}$. Note that the fitted index profile has a relatively small slope at the regions close to the input (air) and the output (silicon) zones, while it varies relatively fast at the region embedded in between. This design coincides with the suggested quantic index profiles shown in [1, 29, 33] obtained by heavy numerical optimizations [30].

4. FEASIBLE SOLUTION TO REALIZE THE MULTILAYER AR DESIGN

Although the ideal index profile is precisely determined in Section 3, the realization is difficult owing to the limitation in natural materials. This dilemma severely cripples the practical performance of the previous designs [14–16] since the dielectrics they found merely have indices close to but not exactly equal to the optimized values. Recently, composite materials that possess high indices of refraction in the THz region have been demonstrated by doping high-index subwavelength-size powders into low-index polymer [27, 28]. These deep-subwavelength-size particles are uniformly distributed inside the host polymer such that the effective refractive index of the composite could be dramatically raised without inducing acute scattering effect. It further implies that versatile polymeric compounds with arbitrary refractive indices ranging between the index of host and that of dopant can be realized by tuning doping ratio. The higher the fraction of dopant, the further the index of composite deviates from that of the host. Giving the doping ratio and the optical properties of host and dopant, the famous Bruggeman's effective medium theory is capable of calculating the resulting refractive index [34]. In 2009, Scheller et al. proposed a modified model [35] to estimate the index of the heterogeneous mixture with consideration of particle shape and the effect of particle-particle interaction. We recall their formula in Eqs. (9) and (10).

$$\zeta = 1 - \left(\frac{n_h}{n_r}\right)^{\left(\frac{-6D^2+6D}{3D+1}\right)} \left(\frac{n_d^2 - n_r^2}{n_d^2 - n_h^2}\right) \times \left[\frac{(1+3D)\,n_d^2 + (5-3D)\,n_h^2}{(1+3D)\,n_d^2 + (5-3D)\,n_r^2}\right]^{\left(\frac{12D-18D^2-2}{9D-12D^2-5}\right)}, \tag{9}$$

$$D = \frac{x_0 y_0 z_0}{2} \int_0^\infty \frac{du}{(x_0^2+u)\sqrt{(x_0^2+u)(y_0^2+u)(z_0^2+u)}}, \tag{10}$$

where ζ represents the volumetric particle fraction (doping ratio); n_h and n_d respectively denote the indices of host and dopant; and n_r is the index of resulting composite. The factor D shown in Eq. (10) is the normalized depolarization factor, in which x_0, y_0, and z_0 are the ellipsoidal axis lengths of dopant.

Several proof-of-principle experiments [27, 28, 35] have already validated this quasi-static effective medium theory by using THz time-domain spectroscopy to characterize the composites, such as linear low-density polyethylene (LLDPE) doped with magnesium hydroxide [$Mg(OH)_2$] and polypropylene (PP) doped with titanium dioxide (TiO_2). They indicated that such model works for the cases of not only low doping ratio but also very high doping ratio due to the particle-particle interaction is included. In the case of PP doped with TiO_2 nano powders [35], the maximum refractive index could achieve 2.985 (for 80% weight doping ratio). However, the attenuation becomes higher than $10\,\text{cm}^{-1}$ for one terahertz owing to the strong dielectric absorption of the dopant. Although the continuous index ranging from 1.567 to 2.985 meets major part of our requirement shown in Table 1, the large attenuation would still reduce the transmission efficiency of multilayer AR coating.

To overcome this problem, low-loss high-density polypropylene (HDPE, $n_h = 1.530 + 4.660 \times 10^{-4}i$ [36]) doped with subwavelength-size high-resistivity silicon powders ($n_d^{\text{Silicon}} = 3.418 + 3.817 \times 10^{-5}i$ [32]) is proposed to realize the high-index layers (for all layers with their $\text{Re}[n_j] \geq 1.530$). On the other hand, it is possible to fabricate the low-index layers (for all layer with their $\text{Re}[n_j] < 1.530$) by doping air pores ($n_d^{\text{Air}} = 1.000$) into the HDPE layer, forming foam structures. The effective medium theory described in Eqs. (9) and (10) is employed to calculate the effective refractive index of the composite as a function of the volumetric doping ratio. In the present calculation, we assume that the shapes of two dopants, i.e., silicon powders and air pores are both spherical, and thus x_0, y_0, and z_0 in Eq. (10) are equal, implying $D = 1/3$. Note that the average diameter of single dopant should be less than $5\,\mu\text{m}$, which is about two orders of magnitude smaller than the free-space wavelength at 0.550 THz ($545\ \mu\text{m}$) to prevent additional scattering loss.

The complex refractive index of low-index (high-index) composite as a function of the volumetric doping ratio of air pores (silicon powers) for layers #1 to #4 (#5 to #10) is illustrated in Fig. 3(a)

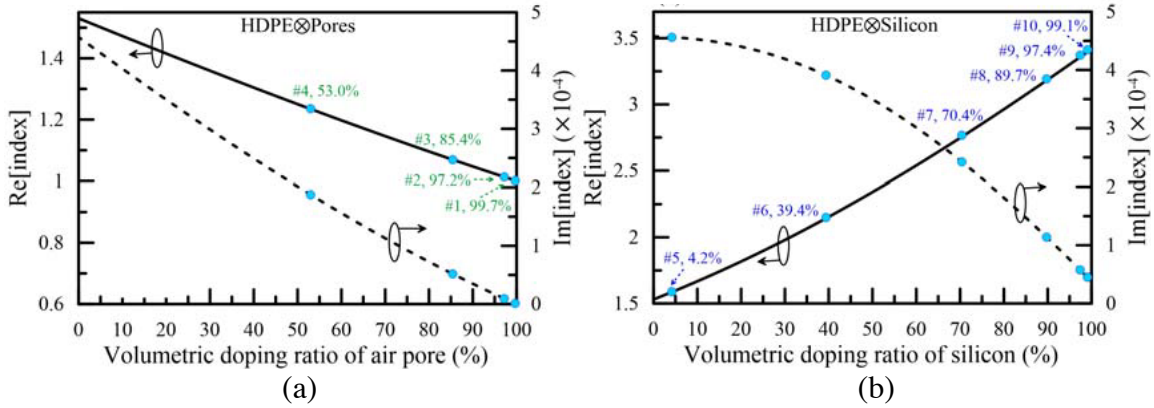

Figure 3. (a) Complex refractive index of porous HDPE as a function of the volumetric ratio of subwavelength-size air pores. (b) Complex refractive index of HDPE-silicon composite as a function of the volumetric ratio of subwavelength-size silicon powders. The refractive index (Re[index]) and the extinction coefficient (Im[index]) are respectively displayed by the black solid curve (refer to the left-hand-side vertical axis) and the black dashed curve (refer to the right-hand vertical axis). The required doping ratios are indicated by the green labels (for relatively low-index layers #1 to #4) in (a) and the blue labels (for relatively high-index layers #5 to #10) in (b).

[Fig. 3(b)]. Note that the suggested recipes (doping ratios) are highlighted by the blue dots in Fig. 3 and retrieved to show in Table 1. Fig. 3(a) shows that the index of porous HDPE layer could be gradually reduced from 1.530 to 1.000 by increasing the fraction of air pores. On the contrary, Fig. 3(b) points out that the index of HDPE-silicon composite can be increased from 1.530 to 3.418 by doping more and more high-index silicon powders. Since the intrinsic absorptions of two dopants employed in this work — air ($\mathrm{Im}[n_d^{\mathrm{Air}}] \sim 0$) and high-resistivity silicon ($\mathrm{Im}[n_d^{\mathrm{Silicon}}] = 3.817 \times 10^{-5}$) are at least order of magnitude less than that of the host polymer ($\mathrm{Im}[n_h^{\mathrm{HDPE}}] = 4.660 \times 10^{-4}$), either the high-index or the low-index composites could exhibit lower dielectric absorption as demonstrated in Fig. 3, facilitating the realization of low-loss multilayer AR coating.

However, the doping ratios of silicon powders for layer #9 and #10 are higher than 90%, which seems difficult to realize by current polymer mixing technique. To conquer the limitation in the manufacture of very high-index layers, this study proposes another two compromise solutions. First, subwavelength silicon-through-hole array (porous silicon) [37, 38] shows potential to fulfill the gap of index > 3. By etching/drilling small hole array with subwavelength period in a silicon wafer, the effective index could be reduced from $\mathrm{Re}[n_{\mathrm{silicon}}] = 3.418$ without increasing loss due to the mix of the small-amount air hole. Second, the TiO_2 nano particles should be reconsidered as the dopant because it possesses a very high refractive index, which achieves 10.486 [35]. Hence, the HDPE-TiO_2 composite layer with effective index greater than 3 can be accomplished under relatively low volumetric doping ratio of TiO_2 ($\zeta \sim 50\%$ [28, 35]), while at the expense of additional dielectric absorption.

On the other hand, the porous HDPE layers can be manufactured by various methods, such as chemical foaming [39], microcellular foaming [40], micro drilling, and femtosecond laser drilling [41]. The typical density of polyethylene foam can be as low as $3 \times 10^{-2}\,\mathrm{g/cm^3}$ (Accuracy Industrial Co., Ltd., Taiwan), implying that the volumetric doping ratio of pores can easily achieve more than 97%. Therefore, layers #2 to #4 are possible to realize by nowadays technology, whereas layers #1 with doping ratio higher than 99% seems infeasible with the consideration of reasonable cost. In what follows, we will demonstrate the performance of ideal ten-layer AR coating, while that of a more feasible design which comprises only layers #2 to #8 (in the absence of layers #1, #9, and #10 due to high difficulty in fabrication) will be displayed for comparison in Section 6.

5. PERFORMANCE OF THE DESIGN AT NORMAL INCIDENCE OF *TE*-POLARIZED WAVE

The AR coating proposed in Section 3 is supposed to remarkably reduce the reflection of THz wave incident from air to silicon, while the multilayer coating with the reverse layer sequence should work for a wave transmitting from silicon to air (by reciprocity). In the following, the overall reflection and transmission of a 375-μm-thick silicon wafer coated with the designed AR coatings on its double sides will be demonstrated. These scattering coefficients under oblique incidence with an arbitrary incident angle (ϕ_0) can be calculated by use of the transfer matrix method (TMM) [42]. It should be noticed that although we neglect all higher-order multiple-reflection echoes in Eq. (1) in order to simplify the design guideline, all of the multiple-reflection events will be considered by TMM. In this section, the performance of the AR coating under normal incidence ($\phi_0 = 0°$) is presented first, while the performance under oblique incidences ($\phi_0 \neq 0°$) for TE-polarized wave (only electric field is parallel to layer interface) and TM-polarized wave (only magnetic field is parallel to the layer interface) will be discussed in Section 7.

Figure 4 displays the overall reflection power ($|\Re|^2$) of the matched system by the red solid curve, while the reflection of the case in the absence of AR coating (defined as an unmatched system) is also illustrated by the black dotted curve for comparison. When a THz wave is directly incident on the silicon wafer, strong Fresnel reflections at air-silicon interfaces result in serious multiple-reflection interference, as manifested in the several on-resonance depths (small reflection due to round-trip constructive interference) and off-resonance plateaus (high reflection due to round-trip destructive interference). While the AR layers are coated on the double sides of the wafer, the reflection is significantly suppressed below the Fresnel reflection (−5.24 dB) from 0.102 THz to 1.031 THz, yielding a 163.99% fractional bandwidth of improvement. Despite the several resonant depths in the reflection spectrum, it is clear that the matched system exhibits much lower reflection and broader bandwidth, in which the minimum reflection (−110.92 dB) appears at 0.562 THz, quite matching the targeted central frequency (0.550 THz). Eq. (7) with $|\Re_{\max}|^2 = 0.300$ (−5.24 dB, Fresnel limit for an air-silicon interface) suggests that the fractional bandwidth of the single-sided AR coating system can achieve 200%. The slight decrease in the bandwidth (163.99%) mainly results from the residual multiple-reflection effect within the silicon substrate.

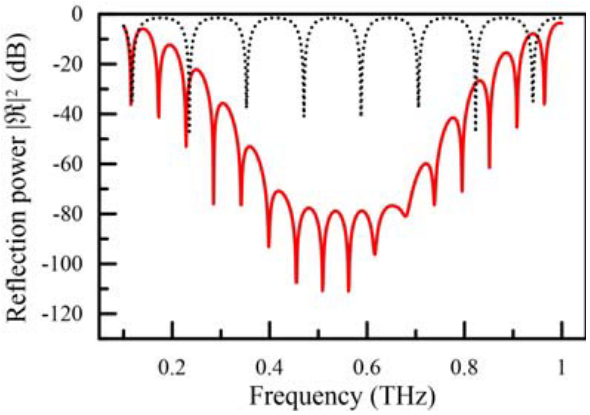

Figure 4. Reflection powers of the unmatched silicon (375-mm-thick wafer alone, black dotted curve) and the well-matched system (375-μm-thick silicon wafer integrated with the designed AR coatings on double sides, red solid curve).

Figure 5(a) demonstrates the overall transmission powers ($|\Im|^2$) for a wave transmitting through the unmatched silicon (black dotted curve) and the matched system (red solid curve). The transmission power of the matched system gets higher than −0.223 dB (95.00%) from 0.203 THz to 0.919 THz, implying an ultra-broad fractional bandwidth of 127.63%. Within this range, the maximum transmission achieves −0.008 dB (99.82%) at 0.115 THz; however, it deviates from the selected matching frequency (0.550 THz). The deviation is attributed to the inclusion of the extinction coefficients of matching layers

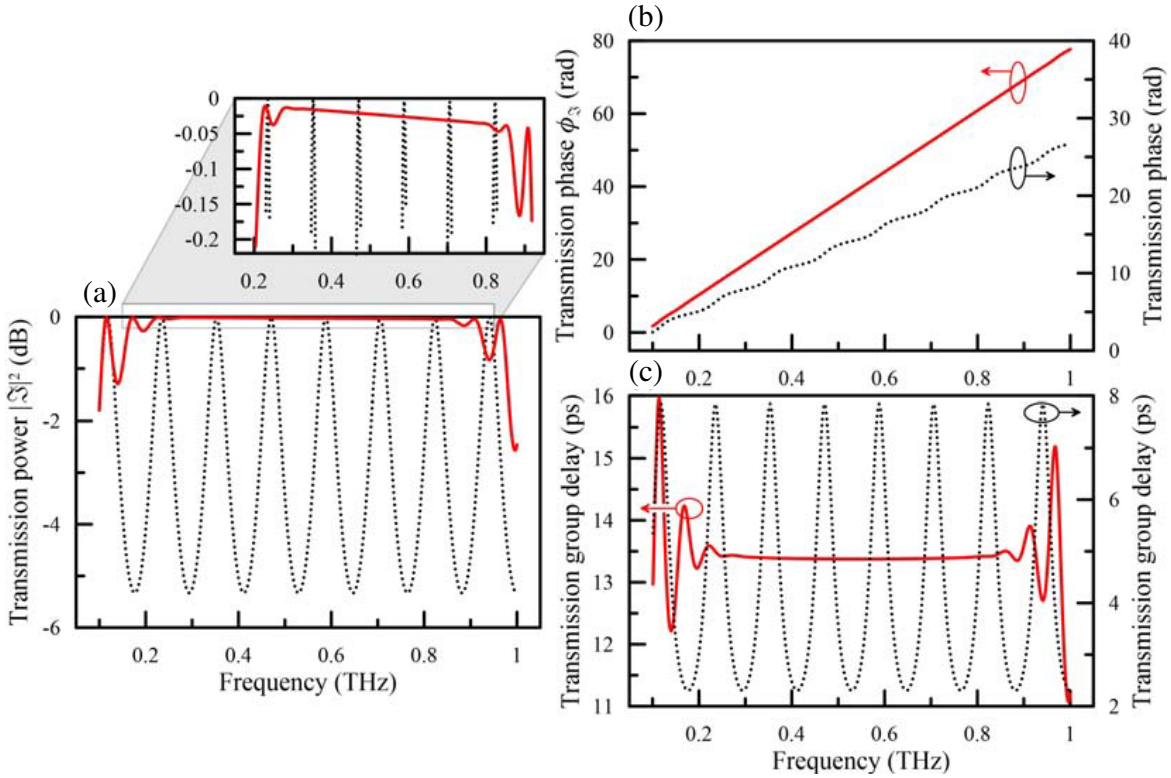

Figure 5. (a) Transmission powers, (b) transmission phase changes, and (c) transmission group delays for the unmatched silicon (black dotted curve) and the matched system (red solid curve). The magnified figure of (a) shows the high-performance band where the transmission power is greater than −0.223 dB (95.00%).

(Im$[n_j]$ listed in Table 1) in the TMM calculation. In other words, when a THz wave passes through the matching layers, it will be slightly dissipated due to the dielectric absorption. The higher the operating frequency, the severer the dissipation, as may be seen from the power attenuation coefficient $\propto$ Im$[n_j] \times \omega/c$. Thus, the lower-frequency component could exhibit better transmission performance, while the transmission power of higher-frequency component would slightly drop down, making the final optimized point for highest transmission (0.115 THz) get a large red shift from the design frequency (0.550 THz).

In addition to transmission power, transmission phase change ($\phi_\Im$) plays an important role in describing the dispersion of a system. For the unmatched case, the ladder-shaped phase change [the black dotted curve in Fig. 5(b)] indicates that the silicon wafer behaviors like a cavity and the injected wave suffers from serious multiple reflections during transmission. On the other hand, the linear phase change for the matched case [the red solid curve in Fig. 5(b)] suggests the disappearance of multiple-reflection interference due to the double-side AR coatings. The transmission group delay shown in Fig. 5(c) is calculated from the first derivate of the transmission phase [Fig. 5(b)] concerning the angular frequency (ω) [43], which represents the overall delay time for the wave passing through the system. For the unmatched system, different frequencies have very discrepant group delays ranging from 2.303 ps to 7.854 ps [the black dotted curve in Fig. 5(c)], indicating strong dispersion. The modulation in transmission group delay with respect to frequency results from the interference between multiple-reflection waves, which modulates the stored field energy in the silicon cavity as well the life time for these energy releasing out [43]. On the contrary, once the multilayer AR coatings are utilized, interface reflection and multiple-reflection interference would be significantly suppressed. The transmission group delay therefore almost stays in a constant around 12.375 ps, implying that the matched system is nearly dispersion-less.

In addition to the frequency-domain performance demonstrated in Figs. 4 and 5, how a composite pulse transmits through the unmatched and the matched systems in time domain is of great interest. According to the Fourier transformation, the frequency-domain transmission coefficient as shown in Figs. 5(a) and 5(b) could construct a complex transfer function $\Im(\omega) \equiv |\Im| \exp(i\phi_{\Im})$ that governs the time-domain behavior for a pulse transmitting through the system in the absence (presence) of the designed AR coatings. With an initial spectrum $S_0(\omega)$, we can describe the time-domain input field $E_{\text{in}}(t)$ and final output field $E_{\text{out}}(t)$ as

$$E_{\text{in}}(t) = \text{FT}^{-1}[S_0(\omega)] \equiv \frac{1}{\sqrt{2\pi}} \int_{-\infty}^{\infty} S_0(\omega) e^{-i\omega t} d\omega, \tag{11}$$

$$E_{\text{out}}(t) = \text{FT}^{-1}[S_0(\omega) \times T(\omega)] \equiv \frac{1}{\sqrt{2\pi}} \int_{-\infty}^{\infty} S_0(\omega) \Im(\omega) e^{-i\omega t} d\omega, \tag{12}$$

in which FT^{-1} represents the inverse Fourier transformation. Without loss of generality, a Gaussian spectrum $\{S_0(\omega) \equiv \exp[-4\ln(2) \times (\omega - \omega_0)^2/\Delta\omega_{\text{FWHM}}^2 + i\omega t_0]\}$ is assigned to the input signal. The central frequency $(\omega_0/2\pi)$ is specified at 0.550 THz, while the full bandwidth at half maximum (FWHM, $\Delta\omega_{\text{FWHM}}/2\pi$) equals 0.170 THz (ranging from 0.465 THz to 0.635 THz), partially covering the operating passband. The initial pulse temporal center (t_0) is selected at 20.000 ps. The transmitted pulses from the unmatched silicon and the matched system are respectively demonstrated in Fig. 6 by the black dotted curve and red solid curve, while the incident pulse is illustrated by the green dashed curve for comparison.

When the injected pulse propagates within the unmatched silicon, it would be split over and over again during the multiple-reflection process, leading to reduction in output peak magnitude and severe waveform deformation. Once the multilayer AR coatings are employed, all interface reflections are dramatically suppressed, resulting in the disappearance of multiple reflections. In other words, the matched system becomes "transparent", such that THz pulse can transmit through it without obvious dissipation and distortion (as shown in the red solid curve in Fig. 6). These two features — ultra-high transmission efficiency and low dispersion clearly show the figure of merit of the present multilayer AR coating.

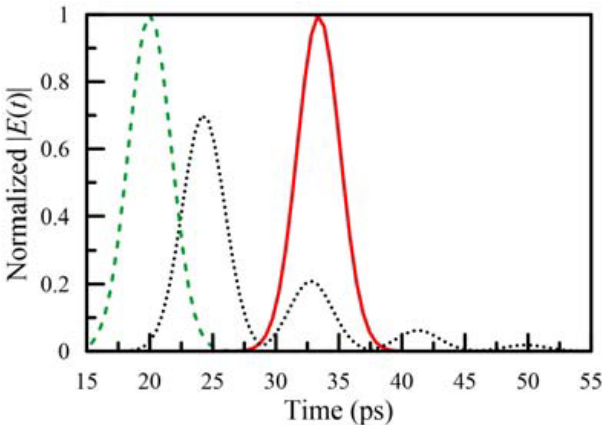

Figure 6. Time-domain field profiles for a broadband Gaussian pulse transmitting through the unmatched silicon (black dotted curve) and the well-matched system (red solid curve). Incident Gaussian profile (assigned as the reference signal) is displayed in the green dashed curve for comparison.

6. SENSITIVITY ANALYSIS AND LIMITATION

As mentioned in Section 4, layers #1, #9, and #10 in the ideal ten-layer design are difficult to manufacture. We, therefore, study a more feasible case composed of layers only #2 to #8, the transmission power of which is demonstrated in Fig. 7(a) by the red dashed curve. As demonstrated,

the fractional bandwidth for $|\Im|^2 > 95\%$ (-0.223 dB) achieves 131.61%, comparable to the performance of the original design. Furthermore, a more realistic situation that includes imperfect contact between adjacent matching layers is considered. The transmission power of a case with 5-μm-thick air gaps lying at all interfaces is illustrated in Fig. 7(a) by the blue dotted curve. Although the fractional bandwidth is still as broad as 128.76% (almost the same as the ideal bandwidth), multiple ripples appear in the original passband (0.203 THz to 0.919 THz), implying the drop of transmission for some frequencies. Fortunately, the maximum drop is only about 2%. It is well to conclude that the absence of edge matching layers (#1, #9, and #10) and the presence of contact gaps (<5 μm) both have a negligible impact on the overall AR performance.

The uncertainties in the manufacturing process, such as losing dopants or polymer hosts might lead to inaccurate volumetric doping ratios (ζ_j), causing unpredictable effective indices (n_j). Here, we analyze the AR performance of two extremes, one of which has matching layers with higher indices (+5%) and the other of which has matching layers with lower indices (−5%) compared to the ideal design values. Their transmission powers are demonstrated in Fig. 7(b). For both extremes, the available bandwidths (> 95% transmission power) are still broader than 120%, while several transmission depths appear in the original flat passband. It is because the ±5% index profiles deviate from the optimized ones given by the binominal approach, which guarantees maximally flat frequency response. Nevertheless, the maximum drop of $|\Im|^2$ is below 1%, indicating that the performance of the AR coating is insensitive to index uncertainty (±5%) of matching layers.

On the other hand, the solidification process of polymer hosts might result in the change of final sample volume, in other words, the layer thickness (d_j) might expand or shrink. The sensitivity of the present AR coating to thickness change thus requires further investigation. Fig. 7(c) plots the transmission power of a case, whose all matching layers are 5% thicker (5% thinner) than the optimized thicknesses in the red dashed (blue dotted) curve. As shown, these two extremes for thickness change not only both reveal flat passbands but also have broad bandwidths comparable to that of the ideal design. Notice that the passband of 5%-thicker (5%-thinner) case has slight red (blue) shift. This can be well explained by the quarter-wavelength condition: $d_j = \lambda_0/(4n_j)$. The thicker (thinner) the layer, the longer (shorter) the effective center wavelength that can satisfy such condition, leading to the red (blue) shift of the whole spectrum.

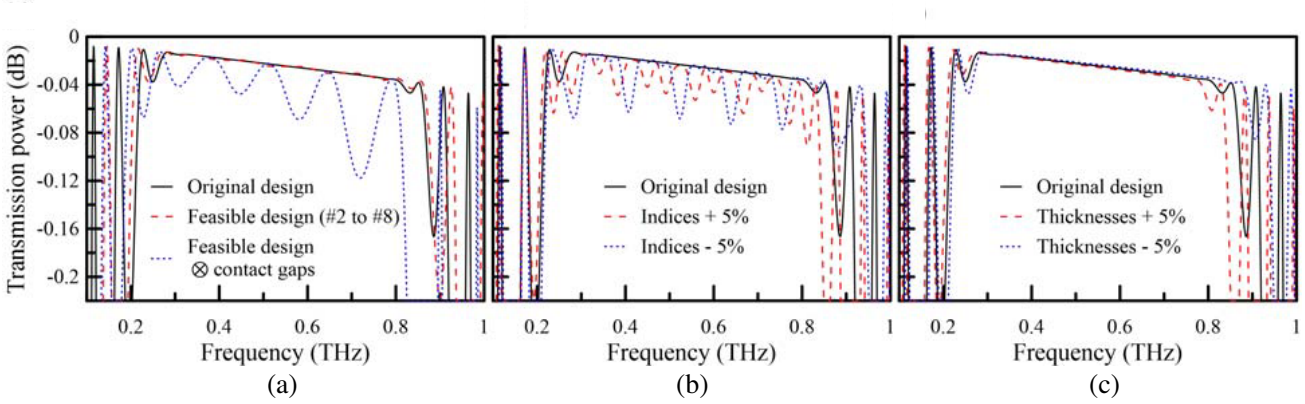

Figure 7. (a) Transmission power of the feasible designs. Red dashed curves: for an AR coating consisting of only layers #2 to #8. Blue dashed curves: for the feasible design (layers #2 to #8) with additional 5-μm-thick contact gaps lying in between all adjacent layers. (b) Sensitivity analysis toward layer indices. Red dashed curve: for the index of every matching layer increasing 5% from the original design. Blue dotted curve: for the index of every matching layers decreasing 5% from the original design. (c) Sensitivity analysis toward layer thicknesses. Red dashed curve: for the thickness of every matching layer increasing 5% from the original design. Blue dotted curve: for the thickness of every matching layer decreasing 5% from the original design. The black solid curves shown in (a), (b), and (c) represent the reference transmission power of the original ten-layer design.

7. PERFORMANCE OF THE DESIGN AT OBLIQUE INCIDENCES OF *TE*-POLARIZED AND *TM*-POLARIZED WAVES

Apart from the normal incidence case ($\phi_0 = 0°$) discussed in Section 5, we expect that the proposed multilayer AR coating is capable of matching air and silicon for both TE-polarized and TM-polarized waves incident at an arbitrary oblique angle ($\phi_0 \neq 0°$). Fig. 8(a) and Fig. 8(b) display the transmission powers at four different angles of incidence ($\phi = 0°$, 20°, 40°, and 50°) for TE polarization and TM polarization, respectively. Although the resonant depths would gradually appear as the incident angle increases, the overall transmission still stays beyond −0.223 dB after 0.250 THz, implying at least 114.46% bandwidth (0.250 THz to 0.919 THz) with more than 95.00% power transmission. Besides, it is clear that the performance of the present AR coating for TM-polarized wave [Fig. 8(b)] is as good as that for TE-polarized wave [Fig. 8(a)]. This suggests that the performance of our AR coating is better than the relief structure proposed in [16].

While the incident angle keeps increasing over 50° [such as 65°, 75°, and 85° as shown in Fig. 9(a) and Fig. 9(b)], the available bandwidth for either TE polarization or TM polarization

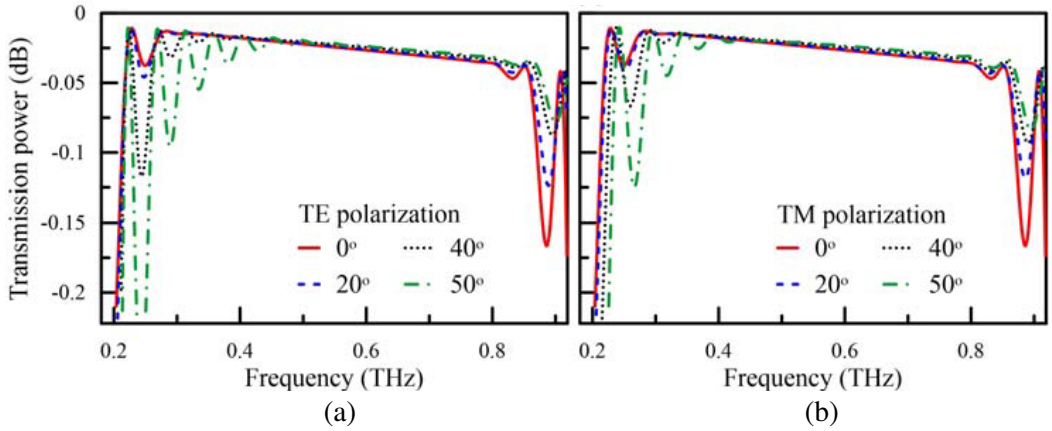

Figure 8. Transmission powers for (a) the TE-polarized and (b) the TM-polarized waves incident at the four different oblique angles [0° (red solid curves), 20° (blue dashed curves), 40° (black dotted curves), and 50° (green dashed-dotted curves)].

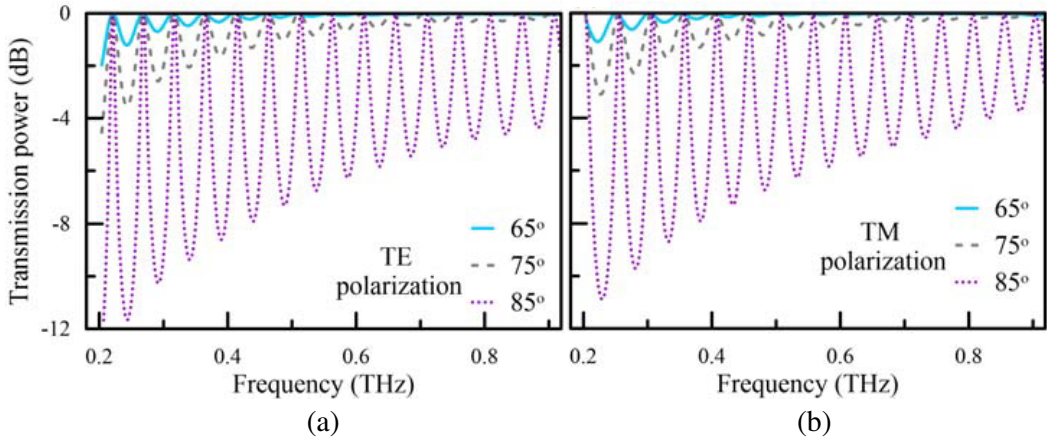

Figure 9. The transmission powers for (a) the TE-polarized and (b) TM-polarized waves incident at the three oblique angles close to grazing incidence [65° (light-blue solid curves), 75° (gray dashed curves), and 85° (purple dotted curves)].

would dramatically decrease due to the appearance of multiple interference depths. The growing of transmission drops with the increase of incident angle can be understood as follows. In oblique incidence [31], the Fresnel reflection at the interface between j-th and $(j+1)$-th layers becomes

$$R_j^{\mathrm{TE}} = \frac{n_j \cos\varphi_j - \sqrt{n_{j+1}^2 - n_j^2 \sin^2\varphi_j}}{n_j \cos\varphi_j + \sqrt{n_{j+1}^2 - n_j^2 \sin\varphi_j}} \quad \text{and} \quad R_j^{\mathrm{TM}} = \frac{n_{j+1}^2 \cos\varphi_j - n_j\sqrt{n_{j+1}^2 - n_j^2 \sin^2\varphi_j}}{n_{j+1}^2 \cos\varphi_j + n_j\sqrt{n_{j+1}^2 - n_j^2 \sin^2\varphi_j}},$$

where φ_j is the incident angle at j-th layer, related to the incident angle at the input zone (ϕ) by Snell's law. The change of Fresnel reflection depends on the incident angle ϕ. The larger the ϕ is, the further the Fresnel reflection at interface deviates from that expected under the normal incidence. For these cases close to grazing incidence, the index profile designed by binominal multi-section approach (Section 2) is no longer valid and "maximally flat frequency response" would disappear. Besides, the traveling route of EM wave inside every matching layer would be significantly prolonged compared to that in the normal incidence. The reflected waves from the adjacent layer-layer interfaces are therefore no longer out of phase, resulting in the serious deviation from the desired destructive interference condition and hence the poor anti-reflection performance. Nevertheless, the present multilayer AR design still shows very good performance for an arbitrary incident angle below 50°, which satisfies the requirement of most applications in the THz range [5–9].

8. CONCLUSIONS

We design a ten-layer anti-reflection coating for widely used silicon wafer in the THz region. The thickness of each matching layer and the refractive index profile are determined based on the guideline of binomial multi-section transformer, while those layers are realized by doping the high-index (silicon) or low-index (air pore) subwavelength-size particles into the host polymer layers (HDPE). The THz transmission power from a 375-μm-thick silicon double-side integrated with the designed AR coating is as high as 95.00% for 0.203 THz to 0.919 THz (127.63% bandwidth) under normal incidence. This performance is superior to not only the monolayer AR coating ($< 20\%$ reflection power with $\sim 30\%$ fractional bandwidth [11]) but also the multilayer AR coating ($< 20\%$ reflection power with $\sim 70\%$ fractional bandwidth [14]) and the sub-wavelength surface-relief structure ($< 20\%$ reflection power with $\sim 60\%$ fractional bandwidth [17]) in the THz regime. On the other hand, the sensitivity analysis suggests that this AR design exhibits strong resistance to both the index and thickness changes of all matching layers, facilitating an easier fabrication procedure. Besides, the proposed AR system works not only for a TE-polarized wave but also for a TM-polarized wave incident from an arbitrary angle below 50°. These features imply that the present design might have multiple further applications in THz windows, THz filters, THz lenses, and semiconductor source devices.

ACKNOWLEDGMENT

This work was supported by National Science Council of the Republic of China, Taiwan, under Grant MOST 104-2112-M-007-007-MY3.

REFERENCES

1. Raut, H. K., et al., "Anti-reflective coatings: A critical, in-depth review," *Energ. Environ. Sci.*, Vol. 4, No. 10, 3779–3804, Oct. 2011.
2. Oh, S. J., et al., "Enhanced broadband and omni-directional performance of polycrystalline Si solar cells by using discrete multilayer antireflection coatings," *Opt. Express*, Vol. 21, A157–A166, 2012.
3. Kaminski, P. M., F. Lisco, and J. M. Walls, "Multilayer broadband antireflective coatings for more efficient thin film CdTe solar cells," *IEEE J. Photovolt.*, Vol. 4, No. 1, 452–456, Jan. 2014.
4. Chhajed, S., et al., "Nanostructured multilayer tailored-refractive-index antireflection coating for glass with broadband and omnidirectional characteristics," *Appl. Phys. Express*, Vol. 4, No. 5, 052503, May 2011.

5. Wagner-Gentner, A., et al., "Low loss THz window," *Infrared Phys. Technol.*, Vol. 48, No. 3, 249–253, Aug. 2006.
6. Lo, S. Z. and T. E. Murphy, "Nanoporous silicon multilayers for terahertz filtering," *Opt. Lett.*, Vol. 34, No. 19, 2921-3, Oct. 1, 2009.
7. Li, Y., et al., "Tunable terahertz-mirror and multi-channel terahertz-filter based on one-dimensional photonic crystals containing semiconductors," *J. Appl. Phys.*, Vol. 110, No. 7, 073111, Oct. 1, 2011.
8. Ito, H., et al., "Continuous THz-wave generation using antenna-integrated uni-travelling-carrier photodiodes," *Semicond. Sci. Technol.*, Vol. 20, No. 7, S191–S198, Jul. 2005.
9. Scherger, B., et al., "Terahertz lenses made by compression molding of micropowders," *Appl. Opt.*, Vol. 50, No. 15, 2256–2262, May 20, 2011.
10. Vlasov, Y., W. M. J. Green, and F. Xia, "High-throughput silicon nanophotonic wavelength-insensitive switch for on-chip optical networks," *Nat. Photon.*, Vol. 2, No. 4, 242–246, Apr. 2008.
11. Gatesman, A. J., et al., "An anti-reflection coating for silicon optics at terahertz frequencies," *IEEE Microw. Guided Wave Lett.*, Vol. 10, No. 7, 264–266, Jul. 2000.
12. Kawase, K. and N. Hiromoto, "Terahertz-wave antireflection coating on Ge and GaAs with fused quartz," *Appl. Opt.*, Vol. 37, No. 10, 1862-6, Apr. 1, 1998.
13. Exter, M. V. and D. Grischkowsky, "Characterization of an optoelectronic terahertz beam system," *IEEE Trans. on Microwave Theory and Tech.*, Vol. 38, 1684–1691, 1990.
14. Hosako, I., "Multilayer optical thin films for use at terahertz frequencies: Method of fabrication," *Appl. Opt.*, Vol. 44, No. 18, 3769–3773, Jun. 20, 2005.
15. Poitras, D. and J. A. Dobrowolski, "Toward perfect antireflection coatings. 2. Theory," *Appl. Opt.*, Vol. 43, No. 6, 1286-95, Feb. 20, 2004.
16. Dobrowolski, J. A., et al., "Toward perfect antireflection coatings. 3. Experimental results obtained with the use of Reststrahlen materials," *Appl. Opt.*, Vol. 45, No. 7, 1555–1562, Mar. 1, 2006.
17. Chen, Y. W., P. Y. Han, and X. C. Zhang, "Tunable broadband antireflection structures for silicon at terahertz frequency," *Appl. Phys. Lett.*, Vol. 94, No. 4, 041106, Jan. 26, 2009.
18. Brückner, C., et al., "Broadband antireflective surface-relief structure for THz optics," *Opt. Express*, Vol. 15, 779–789, 2007.
19. Yang, L., et al., "Hybrid moth-eye structures for enhanced broadband antireflection characteristics," *Appl. Phys. Express*, Vol. 3, No. 10, 102602, 2010.
20. Kim, K.-H. and Q.-H. Park, "Perfect anti-reflection from first principles," *Sci. Rep.*, Vol. 3, 1062, 2013.
21. Huang, Y. F., et al., "Improved broadband and quasi-omnidirectional anti-reflection properties with biomimetic silicon nanostructures," *Nat. Nanotechnol.*, Vol. 2, No. 12, 770-4, Dec. 2007.
22. Yang, J., et al., "Design and fabrication of broadband ultralow reflectivity black Si surfaces by laser micro/nanoprocessing," *Light Sci. Appl.*, Vol. 3, No. 7, e185, 2014.
23. Huang, T.-Y., et al., "Experimental realization of ultrathin, double-sided metamaterial perfect absorber at terahertz gap through stochastic design process," *Sci. Rep.*, Vol. 5, 18605, 2015.
24. Nemati, A., et al., "Tunable and reconfigurable metasurfaces and metadevices," *Opto-Electronic Advances*, Vol. 1, No. 5, 180009, 2018.
25. Babicheva, V. E., et al., "Reflection compensation mediated by electric and magnetic resonances of all-dielectric metasurfaces," *J. Opt. Soc. Am. B*, Vol. 34, No. 7, D18–D28, 2017.
26. Zhang, H., et al., "High-efficiency dielectric metasurfaces for polarization-dependent terahertz wavefront manipulation," *Adv. Opt. Mater.*, Vol. 6, No. 1, 1700773, 2018.
27. Dupuis, A., et al., "Transmission measurements of hollow-core THz Bragg fibers," *J. Opt. Soc. Am. B*, Vol. 28, No. 4, 896–907, Apr. 2011.
28. Ung, B., et al., "High-refractive-index composite materials for terahertz waveguides: trade-off between index contrast and absorption loss," *J. Opt. Soc. Am. B*, Vol. 28, No. 4, 917–921, Apr. 2011.
29. Kuo, M. L., et al., "Realization of a near-perfect antireflection coating for silicon solar energy utilization," *Opt. Lett.*, Vol. 33, No. 21, 2527-9, Nov. 1, 2008.

30. Southwell, W. H., "Gradient-index antireflection coatings," *Opt. Lett.*, Vol. 8, No. 11, 584-6, Nov. 1, 1983.
31. Poza, D. M., *Microwave Engineering*, 3rd Edition, John Wiley & Sons, 2006.
32. Dai, J. M., et al., "Terahertz time-domain spectroscopy characterization of the far-infrared absorption and index of refraction of high-resistivity, float-zone silicon," *J. Opt. Soc. Am. B*, Vol. 21, No. 7, 1379–1386, Jul. 2004.
33. Xi, J. Q., et al., "Optical thin-film materials with low refractive index for broadband elimination of Fresnel reflection," *Nat. Photon.*, Vol. 1, No. 3, 176–179, Mar. 2007.
34. Myroshnychenko, V. and C. Brosseau, "Finite-element modeling method for the prediction of the complex effective permittivity of two-phase random statistically isotropic heterostructures," *J. Appl. Phys.*, Vol. 97, No. 4, 044101, Feb. 15, 2005.
35. Scheller, M., et al., "Modelling heterogeneous dielectric mixtures in the terahertz regime: A quasi-static effective medium theory," *J. Phys. D: Appl. Phys.*, Vol. 42, No. 6, 065415, Mar. 21, 2009.
36. Jin, Y. S., G. J. Kim, and S. G. Jeon, "Terahertz dielectric properties of polymers," *J. Korean Phys. Soc.*, Vol. 49, No. 2, 513–517, Aug. 2006.
37. Ma, L., et al., "Wide-band "Black silicon" based on porous silicon," *Appl. Phys. Lett.*, Vol. 88, No. 17, 171907, 2006.
38. Park, S.-G., et al., "Subwavelength silicon through-hole arrays as an all-dielectric broadband terahertz gradient index metamaterial," *Appl. Phys. Lett.*, Vol. 105, No. 9, 091101, 2014.
39. Li, Q. X. and L. M. Matuana, "Foam extrusion of high density polyethylene/wood-flour composites using chemical foaming agents," *J. Appl. Polym. Sci.*, Vol. 88, No. 14, 3139–3150, Jun. 28, 2003.
40. Gandhi, N. A. A., K. K. Gaur, S. J. A. Rizvi, V. Tiwari, and N. Bhatnagar, "Ultrasound assistedcyclicsolid-statefoamingforfabricatingultra-low density porousacrylonitrile-butadiene-styrene foams," *Mater. Lett.*, Vol. 94, 76–78, 2013.
41. Zhao, X. and Y. C. Shin, "Femtosecond laser drilling of high-aspect ratio microchannels in glass," *Appl. Phys. A*, Vol. 104, No. 2, 713–719, Aug. 2011.
42. Li, Z. Y. and L. L. Lin, "Photonic band structures solved by a plane-wave-based transfer-matrix method," *Phys. Rev. E*, Vol. 67, No. 4, Pt. 2, 046607, Apr. 2003.
43. Winful, H. G., "Group delay, stored energy, and the tunneling of evanescent electromagnetic waves," *Phys. Rev. E*, Vol. 68, No. 1, Pt. 2, 016615, Jul. 2003.